PAPER

Topology-guided deformable registration with local importance preservation for biomedical images

IOP Publishing Phys. Med. Biol. 63 (2018) 015028 (15pp) https://doi.org/10.1088/1361-6560/aa9917

Physics in Medicine & Biology

IPEM Institute of Physics and Engineering in Medicine

PAPER

RECEIVED
21 June 2017

REVISED
18 October 2017

ACCEPTED FOR PUBLICATION
8 November 2017

PUBLISHED
29 December 2017

Topology-guided deformable registration with local importance preservation for biomedical images

Chaojie Zheng[1], Xiuying Wang[1], Shan Zeng[2], Jianlong Zhou[3], Yong Yin[4], Dagan Feng[1,5] and Michael Fulham[6,7]

[1] School of Information Technologies, The University of Sydney, Sydney, Australia
[2] College of Mathematics and Computer Science, Wuhan Polytechnic University, Wuhan, People's Republic of China
[3] Data61, CSIRO, Sydney, Australia
[4] Department of Radiation Oncology, Shandong Tumor Hospital, Jinan, People's Republic of China
[5] Med-X Research Institute, Shanghai Jiao Tong University, Shanghai, People's Republic of China
[6] Department of PET and Nuclear Medicine, Royal Prince Alfred Hospital, Sydney, Australia
[7] Sydney Medical School, The University of Sydney, Sydney, Australia

E-mail: xiu.wang@sydney.edu.au

Keywords: deformable registration, topology guidance, local importance preservation, demons, topology tree

Abstract

The demons registration (DR) model is well recognized for its deformation capability. However, it might lead to misregistration due to erroneous diffusion direction when there are no overlaps between corresponding regions. We propose a novel registration energy function, introducing topology energy, and incorporating a local energy function into the DR in a progressive registration scheme, to address these shortcomings. The topology energy that is derived from the topological information of the images serves as a direction inference to guide diffusion transformation to retain the merits of DR. The local energy constrains the deformation disparity of neighbouring pixels to maintain important local texture and density features. The energy function is minimized in a progressive scheme steered by a topology tree graph and we refer to it as topology-guided deformable registration (TDR). We validated our TDR on 20 pairs of synthetic images with Gaussian noise, 20 phantom PET images with artificial deformations and 12 pairs of clinical PET-CT studies. We compared it to three methods: (1) free-form deformation registration method, (2) energy-based DR and (3) multi-resolution DR. The experimental results show that our TDR outperformed the other three methods in regard to structural correspondence and preservation of the local important information including texture and density, while retaining global correspondence.

1. Introduction

The aim of image registration is to provide an optimal transformation that best aligns corresponding structures of interest from two or more input images, which may be acquired at different times and with different sensors. Biomedical image registration is essential for the fusion of complementary image information from different imaging modalities where fusion may reveal, for example, functional processes overlain on structural data that can assist diagnosis and treatment planning. Image registration is critical in radiation oncology where radiotherapy is directed at a tumor and adjacent normal tissue is spared (Wu *et al* 2008). It also plays an important role in the longitudinal assessment of imaging studies where there can be changes over time related to the underlying condition or changes in the subject's body habitus. Image registration where there are changes or deformations is directed at finding an optimal rigid or non-rigid transformation. Rigid transformation is normally used for registering brain images within a rigid skull (Holden 2008, Rueckert and Aljabar 2010) or as a first step for a more complicated non-rigid/deformable registration. Deformable image registration includes non-physical and physical models.

Non-physical models are derived from interpolation or approximation theory (Sotiras *et al* 2013). In interpolation theory, deformation is considered as a restricted set of known locations in the image, and is interpolated for the rest of the image domain. Free-form deformation (FFD) is a common type of medical image registration.

Dense deformation is given as a summation of tensor products of univariate splines and gained acceptance in medical image analysis when coupled with cubic B-spline (Declerck *et al* 1997, Rueckert *et al* 1999, Kybic and Unser 2003, Sdika 2008). Rueckert *et al* (2006) introduced hard constraints to produce diffeomorphic deformation fields and to preserve topology. Subsequent developments included non-uniform rational B-splines (NURBS) by Wang and Jiang (2007) and multi-level B-spline by Shi *et al* (2012).

Physical models consider the physical characteristics as prior information to constrain the solution space and tissue motion is often modeled as the deformation of an elastic material or viscous fluid (Christensen *et al* 1996, Davatzikos 1997, Al-Mayah *et al* 2011). The finite element method (FEM) is a powerful technique that divides the problem domain into elements and further solves the equations on the element basis. Ahn and Kim (2010) and Hu *et al* (2011) extracted the local image features, such as the object surface, to derive the external forces at the FEM mesh nodes. An adaptive FEM refinement scheme was proposed by Zhang *et al* (2014) for more effective and accurate medical image registration. The diffusion model, 'demons', proposed by Thirion (1998), is another example of a physical model registration. In the demons registration (DR) algorithm, each image is considered as a set of iso-intensity contours with the idea that a regular grid of forces deforms an image by pushing the contours in the normal direction. The orientation and magnitude of the displacements are then derived from the instantaneous optical flow equation. The DR relies on the assumption that pixels representing the same homologous point on an object have the same intensity on the reference and moving images that are to be registered.

The classic DR, which uses image gradient information from the dissimilarity of image intensity, is highly sensitive to local artifacts and can be easily trapped in a local minimum. Variant deformation forces have been proposed to improve the Rogelj and Kovačič (2006) and Wang *et al* (2005) proposed symmetric demons (SymD) algorithms that included gradient information of the moving image and the reference image. In the accelerated 'demons' algorithm an 'active' force, along with an adaptive adjustment of the force strength during the iterative process, was introduced by Wang *et al* (2005) to speed up the registration. Since the DR algorithm moves pixels along the gradient direction, information orthogonal to the direction of the gradient is lost. Lu and Mandal (2010) introduced a symmetric orthogonal gradient to calculate the demons forces and showed that the registration was more accurate. Luo and Chung (2009), instead reported a feature-based image where local intensity histograms were used to substitute the original intensity image. These local histogram-based features are rotation invariant and can capture spatial information. Kroon and Slump (2009) and Modat *et al* (2010) incorporated mutual information into the DR for multimodality registration. Vercauteren *et al* (2009) suggested a diffeomorphic demons (DD) algorithm and it is recognized as a robust and reliable non-rigid method. These investigators combined the DR with the Lie group framework on diffeomorphisms and optimized for the Lie group, instead of performing the optimization on the displacement vector field (DVF) as in the original DR algorithm.

In the DR, the high degrees of freedom (DoF) empowers the deformation model to capture complex image content variations. The underlying registration strategy of the DR is to stimulate the deformation process as a diffusion analogy with thermodynamic concepts. This diffusion mechanism of DR enables its energy function to converge efficiently, but may also result in misalignment under two circumstances: (1) the expected corresponding regions do not overlap; (2) there are overlapping regions with ambiguous correspondence. As shown in figures 1(a) and (b), the circles and the squares are the two expected corresponding pairs, and figure 1(c) displays the situation when the squares do not overlap and when the circle in the moving image has overlapped with the two shapes in the reference image (circumstances 1 and 2 above). The DR (see figure 1(e)) squeezes the moving square, instead of diffusing it into the square of the reference image. It also diffuses the moving circle into the circle and the square in reference image, and therefore results in misregistration. The DR deformation simulates the diffusion process to achieve the registration. However, the freedom of such deformation also introduces variance in local important information including texture and density referred as local importance, which are critical to clinical applications such as radiation therapy.

In this paper, we propose a topology-guided deformable registration (TDR) method to address the fundamental problems with the DR. The TDR has a novel registration energy function that introduces topology energy to guide the demons diffusion process to retain the merits of the DR and preserve the local importance in a progressive registration scheme.

2. Methodology

2.1. DR energy function

Given two images to be registered, a reference image F and a moving image M, the aim of registration is to search for the optimal transformation which deforms points of M onto points of F. Vercauteren *et al* (2007) proposed a standard registration model with a registration energy consisting of a similarity function, a transformation error function, and smoothness regularization. The optical flow equation for finding small deformation in temporal sequences is used as the basis of the DR forces in an iterative process. The squared pixel distance is the similarity

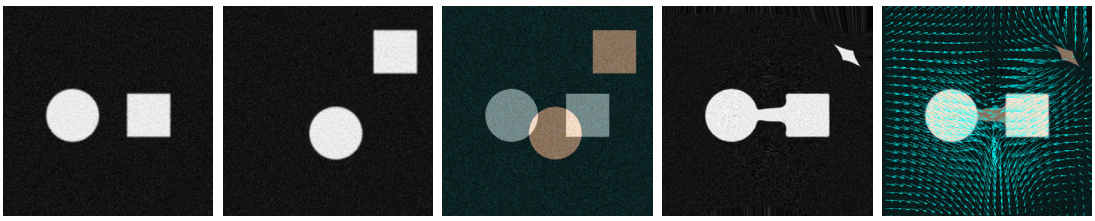

Figure 1. Example of DR registration. (a) Reference image (b) moving image. (c) Fusion of reference and moving images. (d) Moving image after DR. (e) Fusion of reference image and DR result with overlaid deformation field.

measure and the squared transformation field is the transformation regularization. The resulting demons energy can be represented as follows:

$$E_{\text{demons}}(U) = \|F - M \circ (S + U)\|^2 + \frac{\sigma_i^2}{\sigma_x^2}\|U\|^2 \tag{1}$$

where deformation field S describes the translation of every pixel from its original position, with U the (iteration) update of S, σ_i and σ_x the constants for intensity uncertainty (image noise) and transformation uncertainty. Let x and x' be an arbitrary point in F and its corresponding point in M respectively. By minimizing the energy function as in equation (1), The spatial mapping function between the corresponding points in F and M can be formulated by

$$x' = (S + U)(x). \tag{2}$$

2.2. TDR energy function

The DR energy function assumes the homologous dependence on image intensities and derives the diffusion direction based on the local image gradient. However, the diffusion process solely along the image gradient direction may result in an erroneous diffusion direction. Besides, deformation of demons method is derived for each point independently, which may violate the original topology relationship. Hence to overcome these problems with DR, we introduce the topology energy and local importance preservation energy to define a new registration energy function as equation (3).

$$E(U) = E_{\text{demons}}(U) + E_{\text{topo}}(U) + E_{\text{local}}(U) \tag{3}$$

where E_{topo} is the topology energy introduced to guide the diffusion direction derived from demons energy E_{demons} and to find the correspondence by considering the original topology structures. The local importance preservation energy E_{local}, along with E_{topo}, would limit the DoF of transformation freedom to preserve the local topology relations.

2.2.1. Topology energy

Since topological spatial relations are invariant to rotation, translation and scaling transformations, we define a topology energy function to infer topological correspondences for the demons diffusion direction.

2.2.1.1. Topo-tree definition

We aim to derive the 'contain' topological relationship for the internal organs or structures in medical images. Given an image I with regions $\omega_i \subset \Omega_I$, where $i \in N$ is the region index and Ω_I is the domain of image I, we extract topology tree graph G, namely 'topo-tree', to represent the topology relations of the regions. The topo-tree $G = (V, E)$ is defined as an undirected acyclic connected graph with nodes $v_i \in V$ corresponding to each region c_i and edge $e_{ij} \in E \subseteq V \times V$ connecting nodes representing direct 'contain' topology relations between regions. Here, we define that ω_i 'contains' ω_j if $\omega_j \subset \omega_i$ and there exists no region ω_h so that $\omega_h \subset \omega_i \wedge \omega_j \subset \omega_h$. The level of certain node is defined as the length of the path from root to the node with root node v_0 at level 0.

2.2.1.2. Topology regions extraction

To extract the topo-tree graph from a given image, we utilize the histogram thresholding fuzzy C-means (HTFCM) (Siang Tan and Mat Isa 2011) to classify the image into fuzzy clusters due to its capability for automated determination of the numbers of clusters by analyzing the image histogram. We calculate neighborhood connectivity to ensure that disjoint regions can be classified as different regions even when sharing similar intensities. By such, we got the regions set $C = \{\omega_0\} \cup \{\omega_i | 1 \leqslant i \leqslant m\}$, where ω_0 represents image background and m is the number of fuzzy regions.

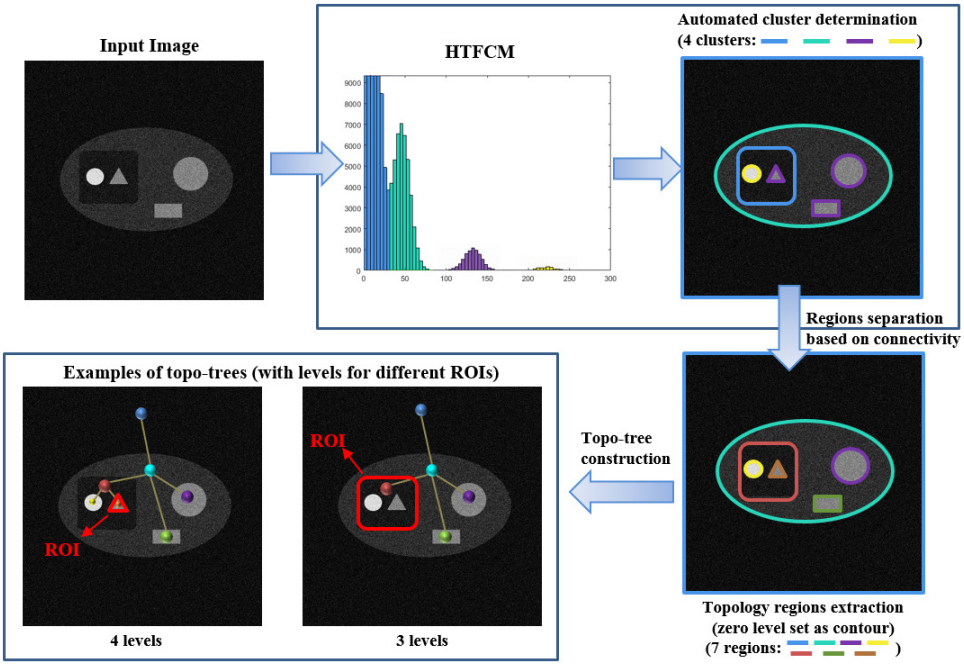

Figure 2. Outline of the automated procedure of topo-tree construction.

2.2.1.3. Topo-tree construction

Given the regions set C, we construct the topo-tree nodes set $V = \{v_0\} \cup \{v_i | 1 \leqslant i \leqslant m\}$ by representing each region ω_i with node v_i, where v_0 stands for the root node representing image background ω_0. Then, we establish edges for nodes with 'contain' relations. The edge establishment starts from root node v_0, and iteratively finds the child nodes for all nodes in V by estimating the topology relation between corresponding regions. If any region ω_i is directly containing ω_j, edge e_{ij} is established and added to the edges set E. The process continues until the topo-tree level reaches the level of node v_{ROI} which is corresponding to the region of interest (ROI) ω_{ROI} specified by user for local importance preservation. The automated topo-tree construction procedure from an input image is illustrated in figure 2.

2.2.1.4. Topology energy derivation

The topology energy E_{topo} is derived from the Euclidean distances of corresponding regions in reference and moving image and the regions are represented by topo-tree nodes. We represent these region distances as signed distance functions (SDF). The contour of region ω, denoted by $c \subset \Omega$, is represented as the zero level set of Lipschitz function $D(x) : \Omega \to R$, such that

$$\begin{cases} c = \partial\omega = \{x \in \Omega : D(x) = 0\} \\ \mathrm{inside}(c) = \omega = \{x \in \Omega : D(x) < 0\} \\ \mathrm{outside}(c) = \Omega \backslash \bar{\omega} = \{x \in \Omega : D(x) > 0\} \end{cases}$$
$$D(x) = \begin{cases} \mathrm{d}(x, \partial\omega) & \text{if } x \in \Omega \backslash \bar{\omega} \\ 0 & \text{if } x \in \partial\omega \\ -\mathrm{d}(x, \partial\omega) & \text{if } x \in \omega \end{cases} \tag{4}$$

where $\mathrm{d}(x, \partial\omega) = \inf_{y \in \partial\omega} \mathrm{d}(x, y)$. Then, for each pixel p, the combined registration energy is formulated as follows:

$$E_{\mathrm{topo}}(u) = \| d_{F,k} - d_{M,k} - u \nabla d_{M,k} \|^2 \tag{5}$$

where $d_{F,k}$ and $d_{M,k}$ are the SDF of the kth corresponding topo-tree nodes or regions where pixel p belongs to in reference and moving images respectively. Then, we can calculate the derivative of E as below:

$$\nabla E_{\mathrm{topo}}(u) = 2(\nabla d_{m,k})^T \left(d_{f,k} - d_{m,k} - u \nabla d_{m,k} \right). \tag{6}$$

Thereby, the registration direction inference is derived from equation (6). Figure 3 illustrates the derivation of topology energy and registration direction inference from topo-tree. As in figure 3, the edge establishment process stops when the topo-tree reaches level 2 where v_{ROI} (the red node) resides.

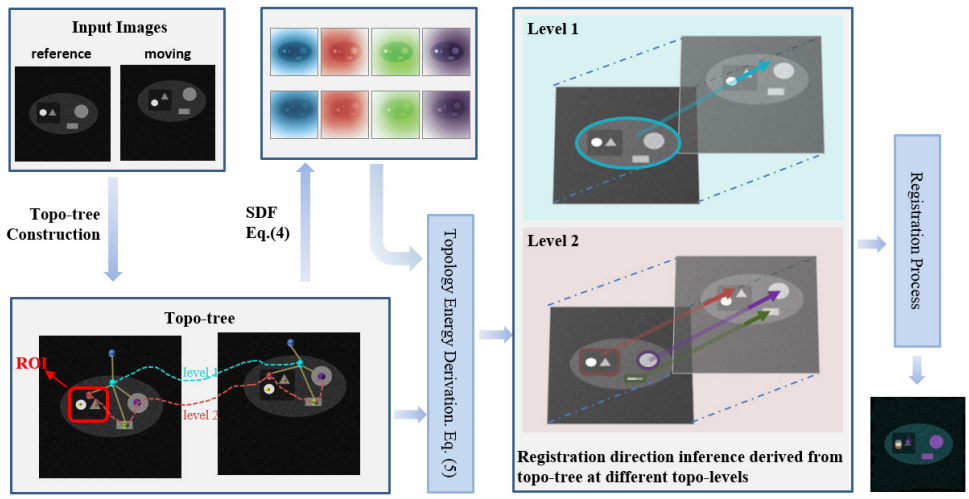

Figure 3. Outline of the derivation of topology energy and registration direction inference.

2.2.2. Local importance preservation energy

The transformation model of DR is a spatial mapping between the corresponding points in M and F. The smoothness of the mapping function is retained through applying a Gaussian kernel. However, due to the physical constraints of an anatomic organ, although the absolute distance of corresponding points may vary significantly under non-rigid registration, the local anatomic structure of a point should be well preserved after deformation. Therefore, it is natural to introduce a local importance preservation energy to constrain the deformation variation of points belongs to the same stiff anatomic structure. Let $\bar{u}_k$ be the mean value of transformation of pixels of same topology region ω_k. The local importance preservation constraint energy for pixel $x \in \omega_k$ can be formulated as:

$$E_{\text{local}}(u) = \text{Var}(u) = E\left[(u-\bar{u}_k)^2\right] = \frac{(u-\bar{u}_k)^2}{N}. \tag{7}$$

Then, we can calculate the derivative of E as below:

$$\nabla E_{\text{local}}(u) = \frac{2(N-1)(u-\bar{u}_k)}{N^2}. \tag{8}$$

Combining the equations (1), (5) and (7), we define the energy function E for each pixel in equation (3) as:

$$\begin{aligned} E(u) &= \alpha\|f-m-u\nabla m\|^2 \\ &+ \beta\|d_{F,k}-d_{M,k}-u\nabla d_{M,k}\|^2 \\ &+ \gamma\left(\frac{(u-\bar{u}_k)^2}{N}+\frac{\sigma_i^2}{\sigma_x^2}\|u\|^2\right) \end{aligned} \tag{9}$$

where f and m are the intensity values of F and M respectively, α, β and γ are the weighting coefficients for demons, topology energy, and local importance preservation energy.

2.3. Optimization of the energy function

The optimization method for a registration framework is the searching algorithm for the optimal deformation. We utilized the L-BFGS (Nocedal 1980), a popular variant of the quasi-Newton approach with less computer memory requirement, to minimize the energy function in equation (9). L-BFGS optimization algorithm updates the deformation vector u at iteration $r+1$ based on the estimation in its previous iteration r as

$$u^{(r+1)} = u^{(r)} - \left(H^{(r)}\right)^{-1} \cdot \nabla E\left(u^{(r)}\right) \tag{10}$$

where the superscript r is the iteration number, $\left(H^{(r)}\right)^{-1}$ represents the approximation of inverse Hessian matrix at iteration r, and ∇ is the gradient operator. Therefore, we need to compute the derivative of the energy function E with respect to u by:

$$\begin{aligned} \nabla E(u) &= 2\alpha(\nabla m)^T(f-m-u\nabla m) \\ &+ 2\beta(\nabla d_{m,k})^T\left(d_{f,k}-d_{m,k}-u\nabla d_{m,k}\right) \\ &+ 2\gamma\left(\frac{(N-1)(u-\bar{u})}{N^2}+\frac{\sigma_i^2}{\sigma_x^2}u\right) \end{aligned}. \tag{11}$$

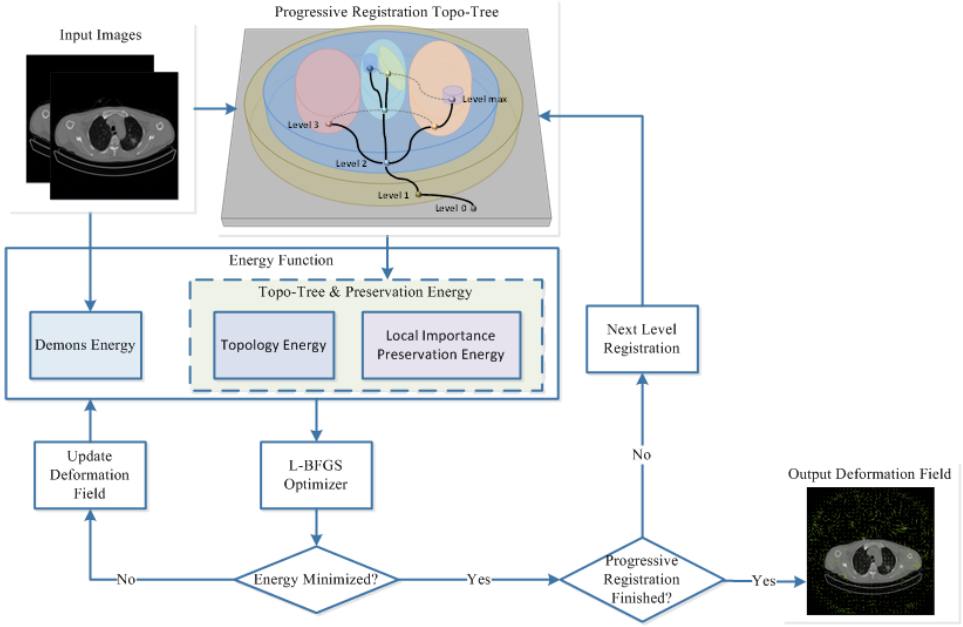

Figure 4. Workflow of progressive registration along the topo-tree.

The L-BFGS optimization is stopped if the difference of objective function value between two consecutive iterations is less than a tolerance value or the iterations reaches a preset maximum iteration number. In our experiments, we set the tolerance and maximum iteration number as 0.01 and 200 respectively.

2.4. Progressive registration along topo-tree

In our TDR method, we introduce the topo-tree which allows the registration to be performed and refined progressively along the tree structure. In figure 4, we outline the workflow of progressive registration on a pair of images along the topo-tree. The topo-tree is extracted from the images and it represents the topology structures of regions in images. Since image background region ω_0 is ineffective in registration process, the corresponding root node v_0 is only used to form the topo-tree graph in a valid tree structure. Therefore, the registration starts from level 1 and it is progressively performed on regions in the next level of the tree until it reaches the maximum level of the tree. While registration is being performed for level l, it treats each region node along with its decedent nodes as a single topology region with preservation of local important features, and each of them contributes to the calculation of energy function $E(u)$ in equation (9) during optimization. In this way, regions of the moving image on level l would be aligned to their corresponding regions in the reference image, and the registration result of their parent regions would be refined due to the effect of the demons energy.

The progressive TDR is summarized below in Algorithm 1:

Algorithm 1. Progressive TDR algorithm.

Input: a pair of images F and M, topo-tree graph G

Output: deformation field U.

for $l \leftarrow 1$ to $l_{\max}$ the maximum level of topo-tree h_G

  Initialize Hessian matrix H

  for $r \leftarrow 1$ to maximum iteration

    vector $g \leftarrow$ gradient of energy function E_l with respect to deformation field $u \in U$

    find a direction p by solving $Hp = -g$

    do line search along p, and update u and g

    if $|g| \rightarrow 0$, convergence criterion is met

      break

    endif

    update H

  endfor

  Interpolate deformation field U on the parent regions of level l

endfor

3. Experiments and results

To evaluate the TDR algorithm, we performed experiments on synthetic image data, phantom PET-CT studies, and clinical PET-CT studies.

3.1. Synthetic image data

20 pairs of synthetic image data were used in our experiments. Each pair of synthetic images contains from one to five corresponding regular shapes. Ten pairs have no overlapping area for corresponding shapes, and the other ten pairs have moving shapes overlapping with incorrect or multiple shapes on reference image. Gaussian noise with 0 mean and 0.3 standard deviation was added to all synthetic data.

3.2. Phantom PET-CT studies

20 lung PET-CT phantom datasets were collected from the public RIDER[8] collections from the Cancer Imaging Archive. The data were based on a NEMA NU-2 IQ phantom (GE Medical Systems using Ge-68) with the central 'lung' cylinder of the IQ phantom removed. The datasets were part of a research plan for measuring the response to drug or radiation therapy and so the decay of the Ge-68 was different between the 20 scans. The target/background ratio was 4:1 with the initial background activity level set to be equivalent to 555 MBq (15 mCi) in a 70 kg patient. The diameters of the 6 spheres were 10 mm, 13 mm, 17 mm, 22 mm, 28 mm and 37 mm. The PET data were reconstructed using a matrix of 128×128 with voxel size $2.73 \times 2.73 \times 3.27$ mm. The CT data were constructed using a matrix of 512×512 with voxels size $0.68 \times 0.68 \times 2.5$ mm. B-spline based artificial deformations were applied to the phantom data to generate the corresponding moving images.

3.3. Patient studies

We analyzed 12 PET-CT studies from patients with non-small cell lung cancer (NSCLC). The scans were carried out on a Biograph TrueV 64 slice PET-CT scanner (Siemens Medical Solutions, Hoffman Estates, IL, USA). PET data were reconstructed into 168×168 matrices with pixel size of 4.07 mm $\times$ 4.07 mm. The CT data were reconstructed using a matrix of 512×512 pixels with pixel size of 0.98 mm $\times$ 0.98 mm. The slice thickness in PET-CT was 2 mm (5 studies) and 3 mm (7 studies). Among the studies, B-spline based artificial deformations were applied to seven of them to simulate the deformation along time. The remaining three studies were temporal data acquired over a 2–4 week interval.

3.4. Validation and comparison methods

We evaluated the performance of our TDR algorithm by comparing the registration results with the following methods: (1) free-form deformable (FFD) registration (Studholme *et al* 2006); (2) energy-based DR (Vercauteren *et al* 2007); (3) multi-resolution DR (MDR) with 4 levels of grid sizes, i.e. from 8×8 to original size 1×1. We assessed accuracy by calculating the mean squared error (MSE) and normalized mutual information (NMI) between the reference and the registered moving image. The MSE is defined as:

$$\mathrm{MSE}\,(F, M) = \frac{1}{n}\sum_{i}^{n}\left(x_{F,i} - x_{M,i}\right)^{2} \tag{12}$$

where F and M are reference and registered images respectively. $x_{F,i}$ and $x_{M,i}$ are ith pixel value of reference and moving images respectively. The minimum MSE value is 0 for two identical images.

The NMI was defined as

$$\mathrm{NMI}\,(F, M) = \frac{H\,(F) + H\,(M) - H\,(F, M)}{H\,(F, M)} \tag{13}$$

where $H\,(F)$ and $H\,(M)$ are Shannon entropies of image F and M respectively, $H\,(F, M)$ is the joint entropy of images. A high NMI value indicates high similarity between images, with maximum 1 indicating a perfect match.

3.5. Experiments on synthetic datasets

Experiments of DR, MDR and TDR on synthetic datasets included evaluations on three categories of registration cases: (1) expected corresponding regions without overlap; (2) relative local position mismatch between corresponding regions; (3) overlapping regions with ambiguous correspondence.

[8] https://wiki.cancerimagingarchive.net/display/Public/RIDER+Collections

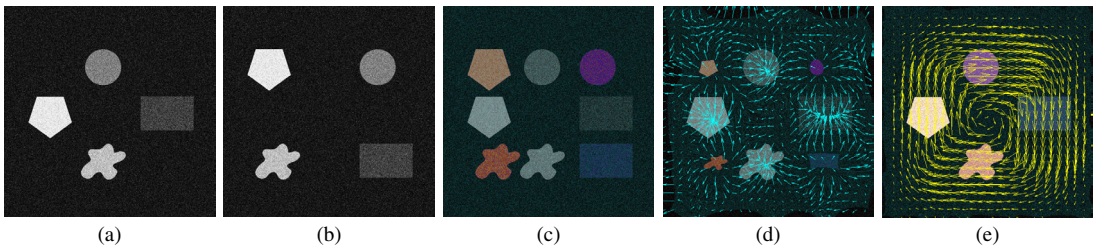

Figure 5. Sample synthetic corresponding regions with gap. (a) Reference image. (b) Moving image. (c) Fusion of reference image (grey) and moving image (color). (d) Fusion of reference image (grey) and MDR result (color) with deformation field. (e) Fusion of reference image and TDR result (color) with deformation field.

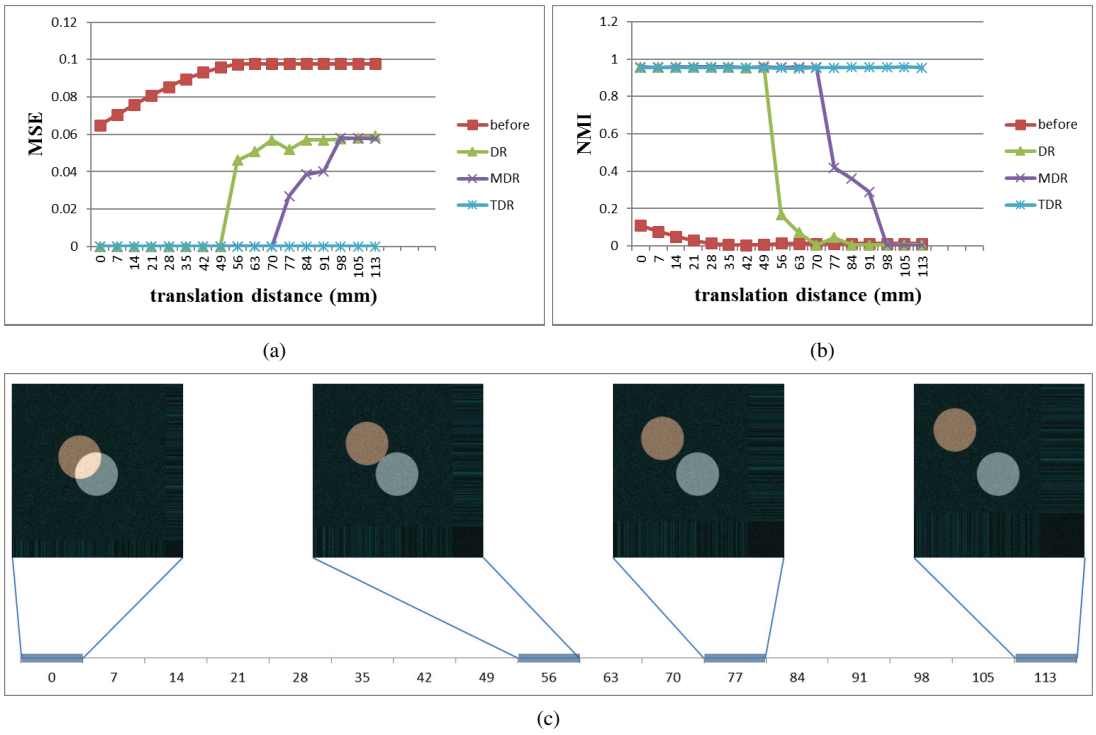

Figure 6. The influence of gap distance on registration result. (a) MSE measurement (b) NMI measurement (c) demonstrations of the degree of misalignment at difference translation distances.

3.5.1. *Expected corresponding regions without overlap*

Figure 5 shows sample registration results for synthetic datasets where clear gaps exist between corresponding regions. There are four shapes to be aligned in the reference and the moving images in figures 5(a) and (b). Since clear gaps existed between corresponding shapes as shown in the fusion image figure 5(c), MDR failed to diffuse the shapes in the moving image into their corresponding region in the reference image as shown in figure 5(d). Instead, it shrank the shapes to compensate for the requirement of total energy minimization. Figure 5(e) shows that the TDR was able to successfully align them.

3.5.2. *Investigation of the influence of gap distance on registration performance*

We further evaluated the influence of the gap distance between corresponding objects on the registration results (see figure 6). We gradually increased the level of misalignment of the circles to be registered by rigidly translating the circle in the moving image away from its original centroid as in the reference image. Then we applied DR, MDR and TDR methods to recover the misalignment, and evaluated the tolerance of these methods. The evaluations are reflected using MSE and NMI criteria, i.e. the lower the MSE and the higher the NMI, the better the registration results. The performance of each method is shown in figures 6(a) and (b) where x-axis is the offset distance and y-axis is the measuring criteria; the performance of the methods could be classified into three intervals, i.e. $[0-56)$ mm, $[56-77)$ mm and $[77-\infty)$ mm. When the distance between centroids was between 0 and 56 mm, the circles overlapped (see figure 6(c)), in which cases all methods were able to align the circles correctly. With the $[56-77)$ mm distance, the circle in the moving image started to disconnect from the circle in the reference, and the MSE and NMI of DR results changed markedly. These findings reflected that

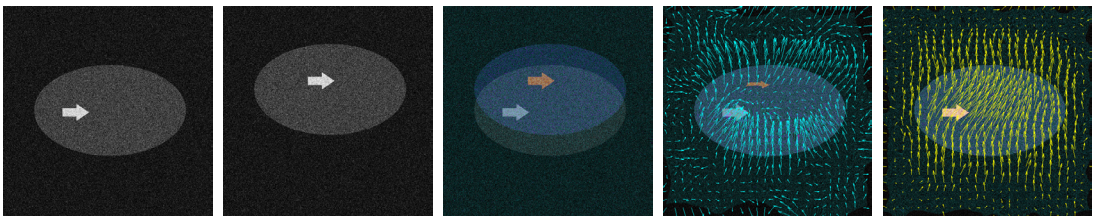

Figure 7. Sample synthetic corresponding regions with an internal gap: (a) reference image, (b) moving image, (c) fusion of reference image (grey) and moving image (color), (d) fusion of reference image (grey) and MDR result (color), (e) fusion of reference image and TDR result (color).

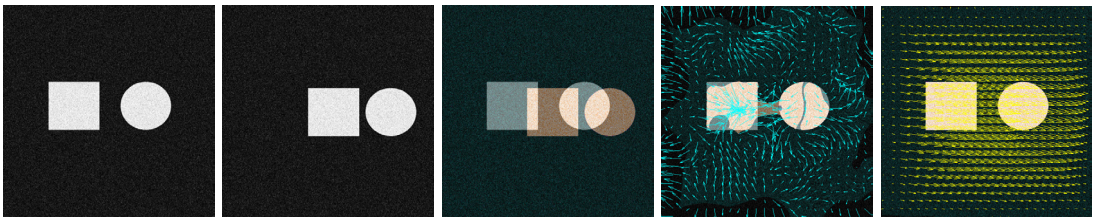

Figure 8. Sample synthetic regions overlapping with multiple regions: (a) reference image, (b) moving image, (c) fusion of reference image (grey) and moving image (color), (d) fusion of reference image (grey) and MDR result (color), (e) fusion of reference image and TDR registration result (color).

the DR method started to fail the registration and was not able to recover the misalignment from then on, while other two methods could register the circles under such circumstances. With the $[77 - \infty)$ mm distance, the gap between circles increased and the MDR method started to fail but the TDR method was able to maintain its accuracy.

3.5.3. Relative local position mismatch between corresponding regions

Figure 7 shows a case where the aim is to align both ellipses and the arrows inside. In reference image figure 7(a), the arrow is located in the left side of the ellipse, while in the moving image figure 7(b), the arrow is in the middle of the ellipse. Figure 7(d) demonstrates that the overlap between the corresponding ellipses enabled MDR to diffuse the ellipse of the moving image into that of the reference image and to correctly align both ellipses. However, the internal arrow was compressed and failed to be aligned to the expected location due to the gap between the arrows. Even if global rigid transformation was applied as a pre-processing step before MDR, there would still be a clear gap between the internal arrows which would result in misalignment. The TDR considered the topology energy as a diffusion guidance and took advantage of the progressive registration scheme to align the ellipses and internal arrows successfully (see figure 7(e)).

3.5.4. Overlapping regions with ambiguous correspondence

Figure 8 outlines a case when one shape in a moving image overlapped multiple shapes in the reference images, including both expected corresponding and uncorrelated shapes. As shown in figure 8(c), the square in the moving image overlapped with the square and the circle in the reference image, and was expected to be aligned with the square in the reference image only. Since both the square and the circle in the reference image had similar intensity values as the square in the moving image, the MDR method diffused the moving square into both shapes as shown in figure 8(d). The TDR method was able to align the square and the circle in the moving image (see figure 8(e)).

3.6. Experiments on phantom datasets

Sample registration results on the PET phantoms are shown in figure 9. Figure 9(c) shows the fusion of the moving image in color and the reference image in grey. The moving image was generated with an artificial warping of the reference image. When compared to the reference image, circle 1 in the left was moved away and detached from the circle in its original location, and circle 2 in the lower left was relocated while keeping attached with the circle in its original location. The left part of the phantom was also deformed to generate more variance. In figure 9(d), the MDR was able to recover the deformation of the left part of the phantom and align circle 2, but was unable to align the circle 1. The MDR also shrank the shape and size of the mis-aligned circle 1 to be almost

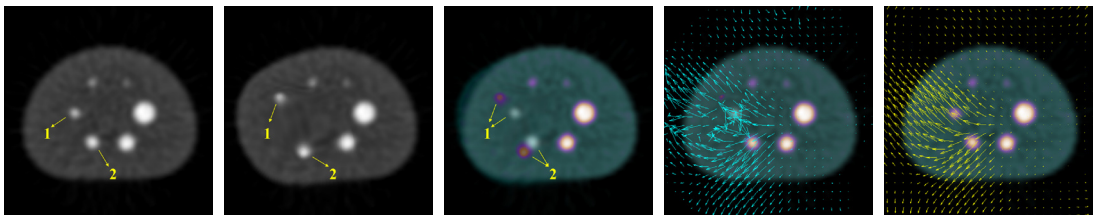

Figure 9. Sample registration results on phantom data: (a) reference image, (b) moving image, (c) fusion of reference image (grey) and moving image (color), (d) fusion of reference image (grey) and MDR result (color), (e) fusion of reference image and TDR registration result (color).

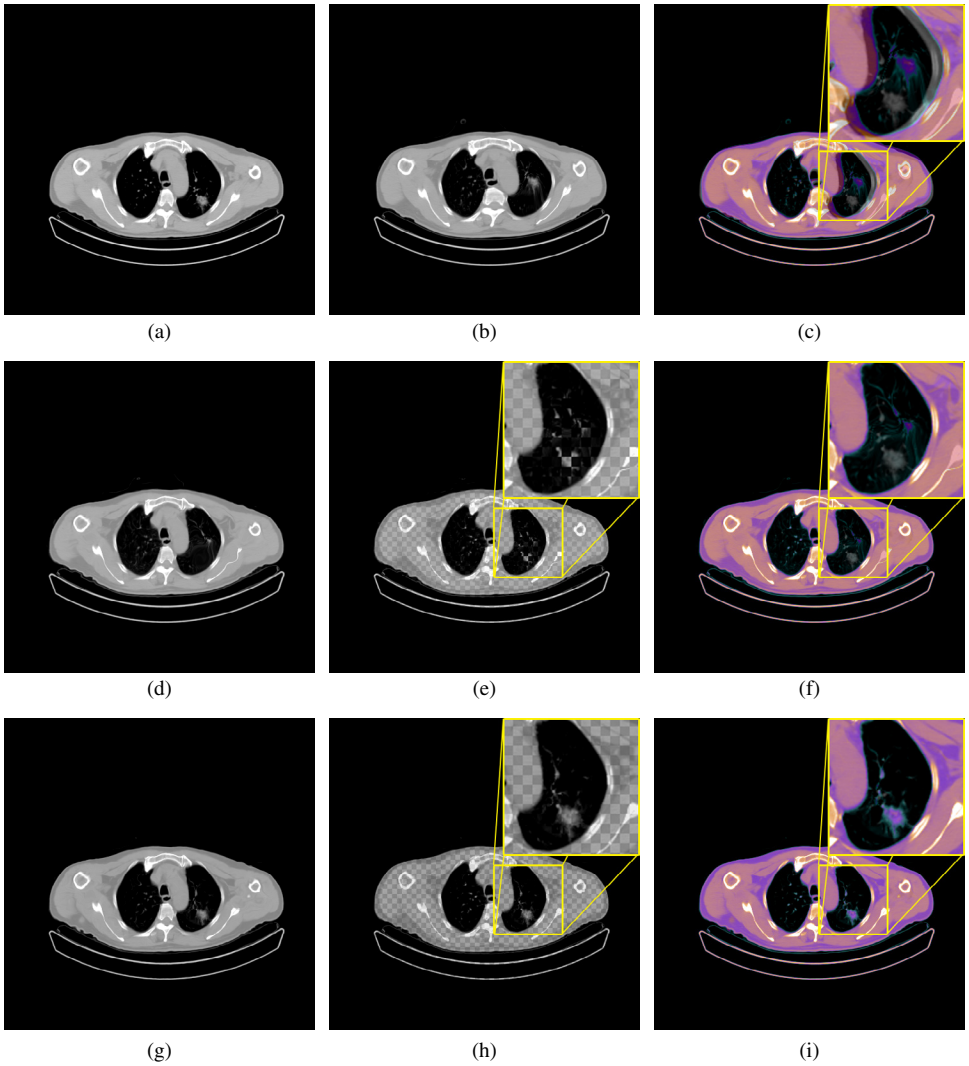

Figure 10. Transaxial chest CT images, using soft tissue windows, with artificial deformation: (a) reference image, (b) moving image with artificial deformation, (c) fusion of reference and moving image, (d) MDR registration result, (e) checker-board view of reference image and MDR registration result, (f) fusion of reference image and MDR registration result, (g) TDR registration result, (h) checker-board view of reference image and TDR registration result, (i) fusion of reference image and TDR registration result.

invisible. The TDR method, figure 9(e), was able to recover the deformation of the phantom equal to that done by MDR, while maintaining the shapes and sizes of the relocated circles and aligning them to their origins.

3.7. Experiments on patient datasets

An example of the registration results for a clinical chest CT scan with synthetic deformation is shown in figure 10. The reference image with a tumor in the left lung is seen in figure 10(a). Artificial deformation was applied to the reference image to generate the moving image which moved the tumor away from its location in the reference image and also affected the left lung and heart (see figure 10(c)). In figures 10(d)–(f) the MDR was able to register

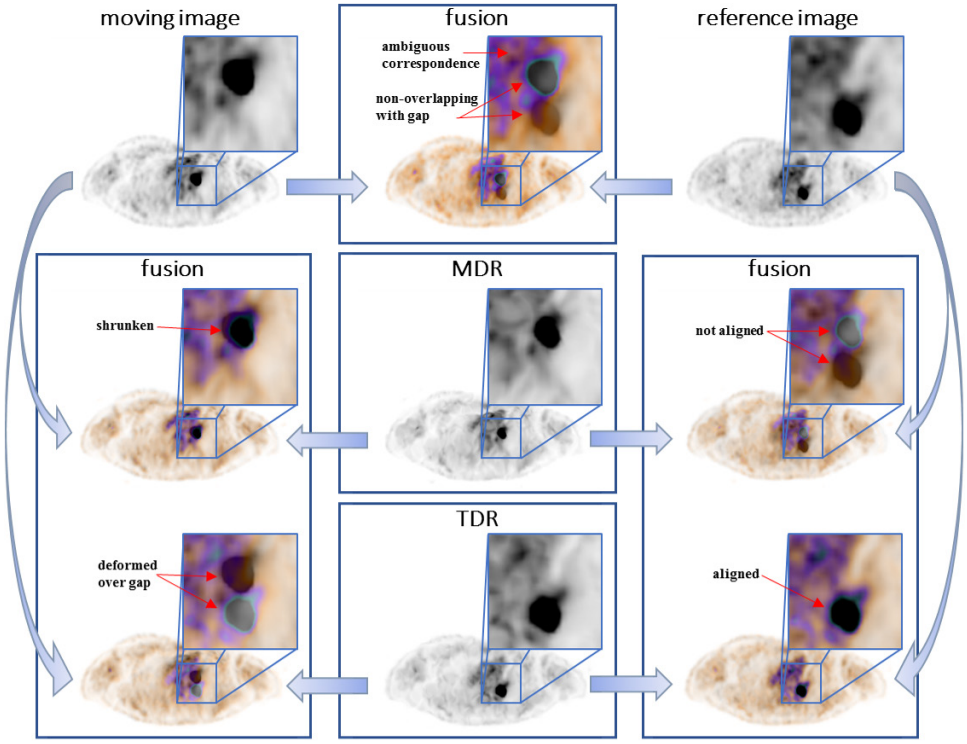

Figure 11. Transaxial PET images of the mid-thorax where a tumor at the left hilum appears as a region of markedly increased glucose metabolism (black region) close to the center of the image.

most of the moving image, e.g. lung and heart, but not the tumor, where it could not detect the correspondence and shrank it to a minimum. In figures 10(g)–(i), the TDR method could perform the global deformation and accurately aligned the tumor to its corresponding location in the reference image.

An example of the registration results on thoracic PET images with synthetic deformation is shown in figure 11. The reference image contained a tumor in the left lung, at the left hilum adjacent to the mediastinum. Artificial deformation moved the tumor away from its location in the reference image and also introduced deformation to the mediastinum, as shown in the image fusion of the moving and the reference images. The fusion MDR result shows that the MDR could not find the corresponding tumor and diffused the tumor into the mediastinum. The fusion TDR, however, could accurately align the tumor to its corresponding location in the reference image and recover the deformation in mediastinum.

3.8. Local importance preservation

We evaluated the volume changes of the ROI after registration to quantitatively measure the effect of the shape deformation after image registration, which is a criterion for treatment response evaluation (Therasse *et al* 2000). In table 1 DR, MDR and FFD had obvious, marked changes on the ROI, i.e. tumor regions in clinical studies, while the TDR method produced minimal changes.

The texture in the tumor region is an important variable in the disease evaluation. As shown in figures 12(a)–(c), besides the offset between the locations of tumors, variations on distribution and shape of standard uptake value (SUV; a semi-quantitative measure of tumor metabolism) could be observed from the moving and the reference images, e.g. the region with maximum SUV (represented in white) in the reference image was much smaller than that in the moving image. The fusion results in figures 12(f) and (i) show that both the DR and the TDR recovered the tumor location offset. However, as shown in figures 12(d) and (g), DR deformed both the shape and SUV distribution of tumor, e.g. the region with maximum SUV (represented in white) is squeezed to match that in the reference image, while the TDR method maintained a similar tumor shape and SUV distribution as that in the moving image.

We evaluated the SUV distribution changes in tumor regions after registration. Figure 13 illustrates this distribution changes on a temporal patient dataset. As shown in figure 13(a), DR deformed the tumor volume and formed a similar distribution trend as the tumor volume in the reference image except for the region with over 90% maximum SUV. The TDR result shared a similar trend as the moving image, but also showed close convergence to the distribution in the moving image in regard to the volume percentage. As shown in figure 13(b), compared to the tumor region in the moving image, the SUV distribution of tumor in the reference image was different, especially for 50%–70% and over 90% maximum SUV regions. The DR deformed the tumor volume

Table 1. Comparison of volume changes (%) on ROI after registration on clinical data.

DR	MDR	FFD	TDR
33.53 ± 15.32	37.76 ± 18.58	25.75 ± 6.43	5.24 ± 3.12

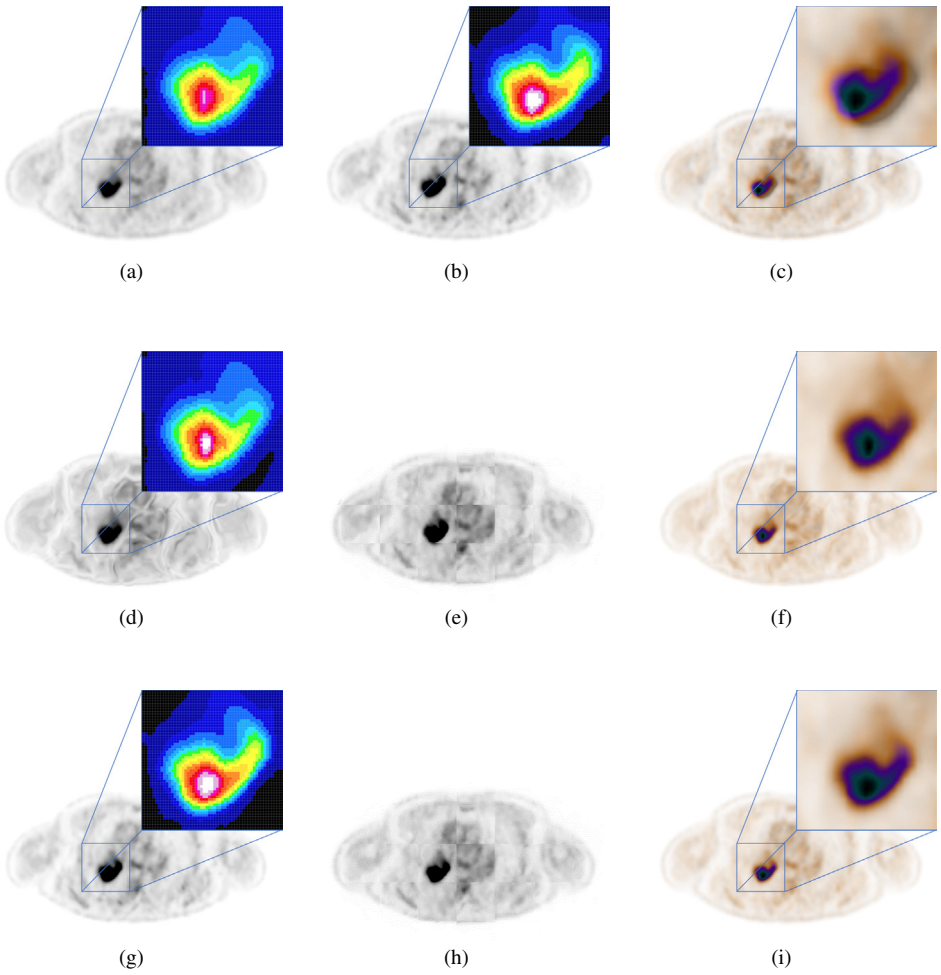

Figure 12. Transaxial thoracic PET images with a tumor (black in the non-zoomed images) located just behind the right hilum with deformable registration effects on tumor region texture from temporal patient data: (a) reference image, (b) moving image, (c) fusion of reference and moving images, (d) DR result, (e) checker-board view of reference image and DR result, (f) fusion of reference image and DR result, (g) TDR result, (h) checker-board view of reference image and TDR result, (i) fusion of reference image and TDR result.

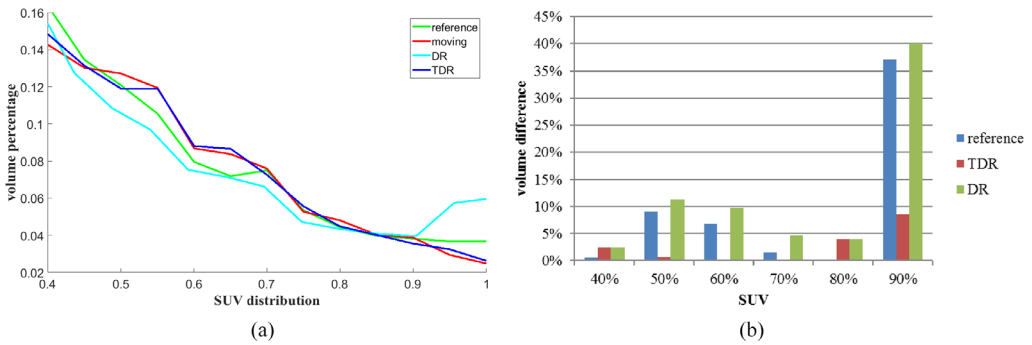

Figure 13. Registration effects on the SUV distribution of tumor regions on moving image: (a) tumor volume distribution at various SUV level, (b) tumor volume distribution difference compared with original moving image.

on the moving image with 50%–70% and over 90% maximum SUV towards a similar volume distribution as the reference image, while TDR method retained the tumor volume distribution and kept the volume difference at a

Table 2. Comparison of global alignment result of MDR, FFD and TDR method.

	Synthetic data (%)		Phantom data (%)		Patient data (%)	
Methods	NMI	MSE	NMI	MSE	NMI	MSE
MDR	92.37 ± 5.13	5.62 ± 3.39	86.77 ± 8.51	7.62 ± 5.94	82.62 ± 7.42	9.72 ± 5.82
FFD	85.46 ± 8.36	9.87 ± 5.53	82.33 ± 9.44	10.86 ± 4.13	77.24 ± 8.65	12.65 ± 7.22
TDR	92.62 ± 6.22	5.56 ± 3.66	86.35 ± 7.72	6.56 ± 3.24	81.21 ± 6.82	9.53 ± 5.74

low level, i.e. less than 5% difference for regions with 40%–90% maximum SUV and 8% changes for regions with over 90% maximum SUV.

3.9. Evaluation of global deformable registration

We calculated the similarity of the reference and deformed moving images using NMI and MSE criteria to validate the global registration efficacy. Since excessive deformation on the texture of a critical regions affects the evaluation criteria, the accuracy of global deformable registration was calculated excluding the tumor area for the phantom and patient studies. Table 2 summarizes the results. Across all three data types, the MDR and the TDR method outperformed the FFD registration. In regard to the quality of the global registration, the performance of TDR was comparable to that of MDR.

3.10. Speed and CPU/memory consumption

We analyzed the speed and CPU/memory consumption of DR, MDR and TDR for clinical data registration on Dell desktop with Intel Core i5-4570 CPU 3.2 GHz, 8 GB memory. All algorithms were implemented in Matlab. As expected, both MDR and TDR showed marked improvement in registration speed in comparison to DR (237.41 ± 5.75 s), while TDR (48.69 ± 5.47 s) was slightly slower than MDR (41.95 ± 4.91 s). It was not surprising that the incorporation of topology energy of TDR method introduced about 16% computation overhead compared to MDR. All three methods required same amount of memory 4.1044×10^4 kb and the optimization process dominated the consumption. As to the CPU consumption, all three methods were in a similar range $74\% - 79\%$.

4. Discussion and future work

Our main findings are that our TDR method is able to correctly register images with non-overlapping corresponding regions, overlapping regions with ambiguous correspondence and preserves locally important variables during registration.

The TDR method, with the incorporation of topology energy, is able to register non-overlapping regions where the classic DR would derive erroneous diffusion directions. The TDR energy function incorporates the topology energy to reflect the topology structure and provides inference to the demons diffusion direction. The topology energy assigns each pixel a general diffusion direction guidance towards its corresponding topology region and the demons energy further tunes the diffusion towards local counterparts around that topology region. Our experimental results (see figures 5, 7, 9–11) demonstrate the contribution of the topology energy to solving the non-overlapping corresponding issue. As shown in figure 6, the MDR eventually failed when the gaps between objects kept increasing when compared to the TDR, which consistently registered the regions regardless of the gap distance.

Our TDR method is also able to solve the problem of registering overlapping regions with ambiguous correspondence (as shown in figure 8) by the introduction of the local importance preservation energy. The local importance preservation energy regulates the deformation and force the diffusion along a similar direction, when a region overlaps with multiple regions and has ambiguous correspondence. In cooperation with the topology energy, the resultant diffusion direction is bound towards a common correspondence. In addition, the local importance preservation energy also serves as a boundary condition during optimization of deformation. Since the structure of the topo-tree is to group pixels based on their topology relationship, the deformation of the outer region infers the deformation of the inner regions. As shown in figure 7, the deformation of the oval inferred the deformation of the inner arrow. Based on the deformation of the oval, TDR deformed the oval and arrow together and then further deformed the arrow to its corresponding area using the topology energy and local importance preservation energy.

The TDR is able to preserve local important information such as texture and density during the registration through the contribution of local importance preservation energy. Since the demons method derives the transformation for each pixel individually regardless of the association with its neighborhood, there is no regulation except for a Gaussian filter utilized to maintain the topology of the pixels and the texture of original images. Such

high DoF of transformation enables the demons method to recover the deformation, while resulting in texture and topology difference from the original images. The local importance preservation energy of TDR maintains the original topology by limiting the disparity of transformation for pixels belonging to same topology region during optimization. Therefore, our topology energy and local importance preservation energy cooperate with demons energy to keep such changes at a low level. Our experimental results (as shown in figure 12) and statistical analysis of SUV distribution difference (as shown in figures 12 and 13) show the local importance preservation capability of TDR.

Since the topo-tree is constructed to describe the relations between topology regions in the image, the intensity levels of the same set of topology regions would not affect the topo-tree structures or the TDR result. For example, in figure 5, the four shapes and the background regions were all of different intensity levels and would derive five clusters corresponding to five topology regions. If the four shapes in figure 5 were assigned the same intensity, the algorithm would derive two clusters including one for the background and the other cluster with the four shapes; and then after calculating the region connectivity, the clusters would be further split into five topology regions. Since both cases would derive the same set of topology regions, the topo-trees of these two cases were exactly the same and which in turn lead to the same topology energy. As there was no other difference in these two cases (except for the intensity settings), the registration results would be similar.

However, the levels of the topo-tree can impact registration results. As shown in figure 2, the topo-tree levels are determined automatically with regard to the ROI for local importance preservation. When choosing different ROIs, topo-trees with different levels will be constructed. Our progressive TDR refines deformation level-by-level and stops at ROI level (the maximum level of the topo-tree), and therefore, no further deformation will be refined for the topology region(s) in the ROI. By such, the TDR results in different registration outputs for different local importance preservations. With regard to the clinical cases, the lesion/tumor region is normally considered as the ROI, and in our experiments, all the procedures were automated once the ROI was given.

Our proposed TDR method is an intensity-based registration that is able to preserve local importance through topological information and relations. Radial basis function (RBF)-based transformations provide a landmark-based registration scheme and are known for their property of topology preservation. RBF-based registration methods optimize the bending energy of landmark displacement, i.e. transformation (Cavoretto *et al* 2014). The RBFs preserve 'neighboring' topology relations through regularizing the transformation in area around landmarks under specified radius. However, as commented upon by Yang *et al* (2011), the performance of RBF not only depends on the possessed topology preservation property of various types of RBF, but also varies according to different spacing between landmarks. Yang *et al* (2011) further indicated that when the displacement of one landmark is bigger enough than its adjacent landmarks, the resultant deformation field could be folded. Therefore, the selection of type and variable radius for RBF would be critical and may affect the registration performance. In comparison with the RBFs which preserve 'neighboring' topology relations, our progressive TDR infers 'contain' topology relations through the topo-tree graph. The integration of such complementary topology relation information would lead to more meaningful registration result. In our future work, we will investigate incorporating the RBF global topology preservation property into our progressive registration scheme.

5. Conclusion

The high DoF of deformation empowers the DR to capture complex image content variations but it is derived from local image gradient information which may result in erroneous deformation, and it lacks explicit correlation among deformation of the neighbouring pixels. We propose a novel registration energy that introduced diffusion guidance for the erroneous demons diffusion direction while retaining the advantages of DR, and preserving important local texture data. Our experimental validation on synthetic, phantom and clinical data show that the introduction of topological information and local importance preservation energy provide more accurate results.

References

Ahn B and Kim J 2010 Measurement and characterization of soft tissue behavior with surface deformation and force response under large deformations *Med. Image Anal.* **14** 138–48

Al-Mayah A, Moseley J, Velec M and Brock K 2011 Toward efficient biomechanical-based deformable image registration of lungs for image-guided radiotherapy *Phys. Med. Biol.* **56** 4701

Cavoretto R, De Rossi A, Qiao H, Quatember B, Recheis W and Mayr M 2014 Computing topology preservation of RBF transformations for landmark-based image registration *Int. Conf. on Curves and Surfaces* (Berlin: Springer) pp 96–108

Christensen G E, Rabbitt R D and Miller M I 1996 Deformable templates using large deformation kinematics *IEEE Trans. Image Process.* **5** 1435–47

Davatzikos C 1997 Spatial transformation and registration of brain images using elastically deformable models *Comput. Vis. Image Understand.* **66** 207–22

Declerck J, Feldmar J, Goris M L and Betting F 1997 Automatic registration and alignment on a template of cardiac stress and rest reoriented SPECT images *IEEE Trans. Med. Imaging* **16** 727–37
Holden M 2008 A review of geometric transformations for nonrigid body registration *IEEE Trans. Med. Imaging* **27** 111–28
Hu Y, Carter T J, Ahmed H U, Emberton M, Allen C, Hawkes D J and Barratt D C 2011 Modelling prostate motion for data fusion during image-guided interventions *IEEE Trans. Med. Imaging* **30** 1887–900
Kroon D J and Slump C H 2009 MRI modalitiy transformation in demon registration *2009 IEEE Int. Symp. on Biomedical Imaging: From Nano to Macro* (*28 June 2009–1 July 2009*) pp 963–6
Kybic J and Unser M 2003 Fast parametric elastic image registration *IEEE Trans. Image Process.* **12** 1427–42
Lu C and Mandal M 2010 Improved demons technique with orthogonal gradient information for medical image registration *IEICE Trans. Inf. Syst.* **E93D** 3414–7
Luo Y and Chung A C 2009 Non-rigid image registration using local histogram-based features *Annual Int. Conf. of the IEEE Engineering in Medicine and Biology Society, 2009. EMBC 2009* (IEEE) pp 5793–6
Modat M, Vercauteren T, Ridgway G R, Hawkes D J, Fox N C and Ourselin S 2010 Diffeomorphic demons using normalized mutual information, evaluation on multimodal brain MR images *Proc. SPIE* **7623** 76232
Nocedal J 1980 Updating quasi-Newton matrices with limited storage *Math. Comput.* **35** 773–82
Rogelj P and Kovačič S 2006 Symmetric image registration *Med. Image Anal.* **10** 484–93
Rueckert D and Aljabar P 2010 Nonrigid registration of medical images: theory, methods, and applications (applications corner) *IEEE Signal Process. Mag.* **27** 113–9
Rueckert D, Aljabar P, Heckemann R, Hajnal J and Hammers A 2006 Diffeomorphic registration using B-splines *Medical Image Computing and Computer-Assisted Intervention–MICCAI 2006* pp 702–9
Rueckert D, Sonoda L I, Hayes C, Hill D L G, Leach M O and Hawkes D J 1999 Nonrigid registration using free-form deformations: application to breast MR images *IEEE Trans. Med. Imaging* **18** 712–21
Sdika M 2008 A fast nonrigid image registration with constraints on the Jacobian using large scale constrained optimization *IEEE Trans. Med. Imaging* **27** 271–81
Shi W, Zhuang X, Pizarro L, Bai W, Wang H, Tung K-P, Edwards P and Rueckert D 2012 Registration using sparse free-form deformations *Int. Conf. on Medical Image Computing and Computer-Assisted Intervention* (Berlin: Springer) pp 659–66
Siang Tan K and Mat Isa N A 2011 Color image segmentation using histogram thresholding—fuzzy C-means hybrid approach *Pattern Recognit.* **44** 1–15
Sotiras A, Davatzikos C and Paragios N 2013 Deformable medical image registration: a survey *IEEE Trans. Med. Imaging* **32** 1153–90
Studholme C, Drapaca C, Iordanova B and Cardenas V 2006 Deformation-based mapping of volume change from serial brain MRI in the presence of local tissue contrast change *IEEE Trans. Med. Imaging* **25** 626–39
Therasse P *et al* 2000 New guidelines to evaluate the response to treatment in solid tumors *J. Natl Cancer Inst.* **92** 205–16
Thirion J P 1998 Image matching as a diffusion process: an analogy with Maxwell's demons *Med. Image Anal.* **2** 243–60
Vercauteren T, Pennec X, Perchant A and Ayache N 2007 Non-parametric diffeomorphic image registration with the Demons algorithm *Medical Image Computing and Computer-Assisted Intervention—MICCAI 2007: 10th Int. Conf. Proc. Part II (Brisbane, Australia, 29 October–2 November 2007)* ed N Ayache *et al* (Berlin: Springer)
Vercauteren T, Pennec X, Perchant A and Ayache N 2009 Diffeomorphic demons: Efficient non-parametric image registration *Neuroimage* **45** S61–72
Wang H, Dong L, O'Daniel J, Mohan R, Garden A S, Ang K K, Kuban D A, Bonnen M, Chang J Y and Cheung R 2005 Validation of an accelerated 'Demons' algorithm for deformable image registration in radiation therapy *Phys. Med. Biol.* **50** 2887–905
Wang J and Jiang T 2007 Nonrigid registration of brain MRI using NURBS *Pattern Recognit. Lett.* **28** 214–23
Wu Z, Rietzel E, Boldea V, Sarrut D and Sharp G C 2008 Evaluation of deformable registration of patient lung 4DCT with subanatomical region segmentations *Med. Phys.* **35** 775–81
Yang X, Xue Z, Liu X and Xiong D 2011 Topology preservation evaluation of compact-support radial basis functions for image registration *Pattern Recognit. Lett.* **32** 1162–77
Zhang J, Wang J, Wang X and Feng D 2014 The adaptive FEM elastic model for medical image registration *Phys. Med. Biol.* **59** 97